Carbon 158 (2020) 55–62

Contents lists available at ScienceDirect

Carbon

journal homepage: www.elsevier.com/locate/carbon

Rapid soldering of flexible graphene assembled films at low temperature in air with ultrasonic assistance

Huaqiang Fu [a], Yong Xiao [a, *], Rongguo Song [b], Zhe Wang [b], Hongjun Ji [c], Daping He [b, **]

[a] School of Materials Science and Engineering, Wuhan University of Technology, Wuhan, 430070, China
[b] Hubei Engineering Research Center of RF-Microwave Technology and Application, Wuhan University of Technology, Wuhan, 430070, China
[c] Flexible Printing Electronic Technology Center, Harbin Institute of Technology at Shenzhen, Shenzhen, 518055, China

ARTICLE INFO

Article history:
Received 8 October 2019
Received in revised form
24 November 2019
Accepted 28 November 2019
Available online 29 November 2019

ABSTRACT

Gaphene assembled film (GAF) has shown great potentials in practical applications. However, it is still a big challenge to reach reliable soldering of GAF at low temperature, and overcome the exfoliation tendency and the electrical loss resulted from anisotropy of GAF. In this work, we developed a rapid low temperature soldering process for GAF inspired by an ultrasonic assistance technology. As a result, Sn solder spots were prepared on the surface of GAF by ultrasonic metallizing treatment for 10 s in molten Sn at 300 °C. The shock waves and micro-jets induced by ultrasonic waves were supposed to improve the poor wettability of GAF, which propelled molten Sn to penetrate into GAF interlayers, and drove Sn atoms to impinge GAF surface to form an amorphous carbon (a-C) layer at GAF/Sn bonding interface. Specially, the penetration bonding between GAF and Sn solder could not only overcome the exfoliation tendency of GAF, but also reduce the electrical loss between GAF interlayers. The GAF/Sn/GAF soldered joints prepared by remelting Sn metallization layers exhibited excellent tensile resistance and electrical conductivity. Such efficient and reliable soldering technology can facilitate the development of high-performance carbon-based materials in electronic industry.

1. Introduction

Graphene assembled film (GAF), which is composed of highly oriented stacking graphene multilayers, exhibits superflexibility, high electrical conductivity and light weight [1–3]. Thus, GAF displays great potentials in electronic devices [4] such as sensors [5,6], detectors [7,8], capacitors [9,10], antennas [11–13], light-emitting electrical conductors [14] and so on. For the fulfilment of assembly and design of GAF electronic devices, appropriate connection techniques are essential to combine GAF with other workpieces [15]. Simultaneously, considering the using environment of GAF assemblies, the GAF joints should meet the requirement of high structure stability and high electrical conductivities. However, with its stacked structure of graphene multilayers, GAF displays anisotropy involving interlayer exfoliation tendency [16] and low electrical conductivity between GAF interlayers [17], which would reduce the connection performance. Therefore, a connection methodology to reliably connect GAF with other workpieces is desired, yet challenging.

The approaches for the connection of GAF, with few reports, can be classified into two categories involving physical connection and metallurgical connection. Physical connection was usually realized by adhesive bonding [12,18] such as silver conductive adhesive (SCA), but the overall performance of GAF device including mechanical property and electrical conductivity was dramatically degraded because of anisotropy of GAF and lower electrical conductivity of adhesive agent [19,20]. In terms of metallurgical connection, it occures at atomic scale, and can significantly enhance connection performance [21–23]. Metallurgical connection could be realized by electrical Joule welding, but this method was confined to connect graphene assemblies themselves, and the shear strength of GAF joints prepared with this method was only 72 KPa [23]. Brazing or soldering technique which can achieve metallurgical connection for the same or dissimilar workpieces may serve as a promising connection methodology for GAF devices [24–27]. However, strong C–C bonding in GAF would result in an obstacle to forming metallurgical connection [28,29], which was

* Corresponding author.
** Corresponding author.
E-mail addresses: yongxiao@whut.edu.cn (Y. Xiao), hedaping@whut.edu.cn (D. He).

https://doi.org/10.1016/j.carbon.2019.11.089
0008-6223/

generally overcome by offering high temperature [30,31] and high pressure [32–34] environment, as well as extending of connection time [35,36] during brazing or soldering. Thus, regular brazing or soldering methods are limited during practical fabrication process. Notably, the negative coefficient of thermal expansion (CTE) of GAF mismatches the CTE of brazing alloys [37,38], which could generate high residual stress and reduce connection performance under high brazing temperature [39]. Furthermore, regular brazing techniques can only offer exterior connection for GAF surface, there still exist exfoliation tendency and electrical loss between GAF interlayers. Therefore, it is still a big challenge to rapidly reach metallurgical connection for GAF at low temperature, coupled with overcoming the exfoliation tendency and the electrical loss resulted from anisotropy of GAF so far.

Herein, we proposed a rapid soldering process for GAF with ultrasonic assistance at low temperature in air. Pure Sn solder spots tightly connected with GAFs were prepared on GAF surface after ultrasonic metallizing treatment for 10 s in molten Sn at 300 °C. With ultrasonic assistance, shock waves and micro-jets induced by ultrasonic waves were supposed to improve the poor wettability of GAF, which propelled molten Sn to penetrate into GAF interlayers to form a ramified structure of GAF. And Sn atoms were diven to impinge GAF surface to form an amorphous carbon (a-C) layer at Sn/GAF bonding interface, resulting in the formation of a smooth transition of lattice from GAF to Sn, and the mediating of the CTE mismatch between GAF and Sn solder. Moreover, compared with exterior bonding between GAF surface and SCA, the penetration bonding between GAF and Sn solder could not only overcome the exfoliation tendency of GAF, but also reduce the electrical loss between GAF interlayers. The GAF/Sn/GAF soldered joints prepared by remelting Sn metallization layers displayed excellent tensile resistance and electrical conductivity. In addition, we found that the GAF/Sn/GAF soldered joints were of high stability after high temperature and aging treatments. Such an efficient and reliable soldering technology can contribute to further development of high-performance carbon-based materials devices in electronic industry.

2. Experimental

2.1. Preparation of GAF

Firstly, the graphene oxide (GO) purchased from Wuxi Chengyi Education Technology Co., Ltd. was diluted with ultrapure water to obtain a GO suspension with a density of 5–20 mg/mL. Secondly, the GO suspension was mechanically stirred to a gel state and then coated on a base PET film, after evaporation dryness a GO film was obtained. Thirdly, the GO film was annealed at 1300 °C for 3 h and then 3000 °C for 1 h in a high temperature furnace under argon atmosphere. Finally, a rolling process was implemented to obtain a flexible graphene assembled film with a thickness of 25 μm.

2.2. Ultrasonic surface metallizing and soldering process of GAF

Before ultrasonic surface metallizing treatment, each piece of GAF was cut into the size of 5 mm × 15 mm by laser. For ultrasonic surface metallizing process, as shown in Fig. 1, the Sn solder spot was prepared by immersing the bottom of GAF into molten Sn at 300 °C in air with ultrasonic vibration for 10 s (the vibration time was selected by contrast experiments as shown in Fig. S1 in supporting information). The GAF/Sn/GAF soldered joints were fabricated by remelting Sn solder spots on the surface of GAFs (the remelting process can be seen in Fig. S2 in supporting information).

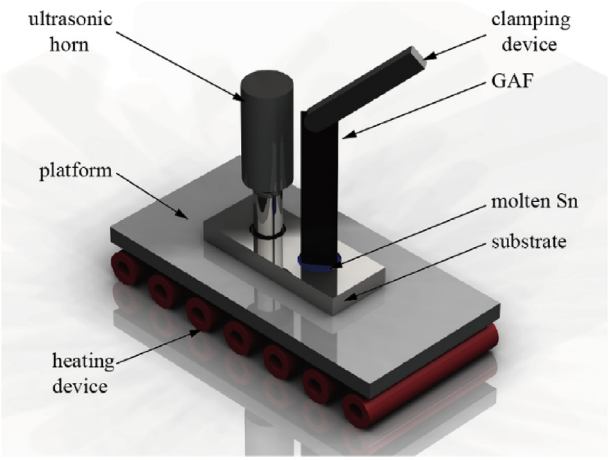

Fig. 1. Schemetic diagram of ultrasonic surface metallizing process of GAF. (A colour version of this figure can be viewed online.)

2.3. Characterizations and tensile test

Scanning electron microscopy (SEM) images were taken on a Zeiss Ultra Plus Field emission scanning electron microscope. Raman spectra of GAF was measured using an excitation wavelength of 457.9 nm provided by a Spectra-Physics Model 2025 argon ion laser. Data of X-ray diffraction (XRD) were collected with a D8 advance diffractometer. TEM samples were prepared by the focus ion beam (FIB) system in Nova NanoSEM 450 scanning electron microscope. Transmission electron microscope (TEM) characterizations were carried out on a Titan G2 60–300 Probe Cs Corrector high-resolution scanning transmission electron microscopy (HRSTEM). The tensile test was carried out in an electromechanical universal testing machine (E44.104) with a crosshead speed of 0.1 mm/min. At least three samples were tested for each kinds of GAF joints, then the average value of tensile breaking force was obtained.

3. Results and discussion

As shown in Fig. 2a, the GAF is of high flexibility, and it can keep structural integration and stable conductivity (Figs. S3a–d, Supporting Information) after repeated bending and folding. The surface of GAF with numerous granular bubbles and microfolds is rough (Fig. 2b), and the measured maximum height difference of GAF surface is 13.61 μm (Fig. S4, Supporting Information). Fig. 2c shows that the GAF is composed of highly oriented stacking graphene multilayers. Fig. 2d shows the Raman spectra of GAF. The I_D/I_G ratio is 0.01637, indicating that the GAF presents a high graphitization degree. Since The G-band peak at 1580 cm-1 is the fingerprint of high crystalline graphite, and the D-band peak reveals the disorder degree of GAF [40,41]. Fig. 2e displays the X-ray diffraction (XRD) pattern of GAF. The sharp and intense diffraction peaks of GAF are obvious, in which the peak of (0 0 2) plane located at around 26.5° demonstrates regular stacked graphene multilayers with an interlayer spacing of 0.34 nm. Combining with the strong peak of (0 0 4) plane, the XRD pattern reflects high degree graphitization of GAF [12]. Fig. 2f displays the HRTEM image of GAF cross-section. The interlayer spacing of 0.34 nm is consistent with the C (0 0 2) peak in Fig. 2e. The selected area electron diffraction (SAED) pattern of GAF (inset image in Fig. 2f) presents as a dot matrix of single crystal, which further manifests the oriented stacked structure of GAF.

Rapid soldering of GAF at low temperature in air was realized by

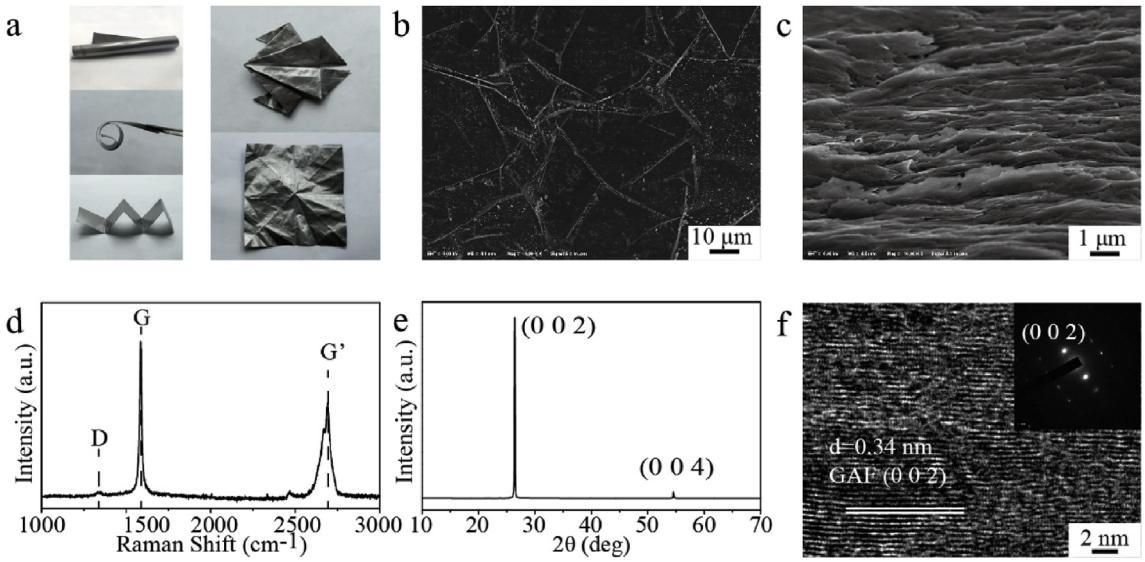

Fig. 2. Characterization of GAF. (a) Bending, folding states of flexible GAF, and GAF was folded into a shape of frog without breakages left. (b) SEM image of GAF surface. (c) SEM image of GAF cross-section. (d) Raman spectra of GAF. (e) XRD patterns of GAF. (f) HRTEM image and SAED patterns of GAF cross-section. (A colour version of this figure can be viewed online.)

ultrasonic metallizing, which could quickly prepare a Sn solder spot tightly connected to GAF. Fig. 3a shows the cross-section image of Sn solder spot on GAF surface. With the assistance of ultrasonic waves, molten Sn can penetrate into interlayers of GAF to form ramified structure of GAF. Fig. 3b and c shows the rough GAF/Sn interfaces and good combination between GAF and Sn solder spot. Simultaneously, many graphene nanosheets are exfoliated from GAF and flowed into Sn solder spot.

Generally, Sn solder performs poor wettability on GAF surface due to different bonding mechanism [42,43]. However, with the help of ultrasonic waves, Sn can spread on the surface of GAF and form good combination with GAF. Fig. 3d illustrates the formation principle of Sn solder spot on GAF. During the ultrasonic surface metallization process, high intense ultrasonic waves are inducted into molten Sn. Acoustic cavitation effects, which include the formation, growth and implosive collapse of vacuum collapse [44] may be formed near the molten Sn/GAF interface. This may induce the formation of shock waves and liquid micro-jets, which can increase the kinetic energy of Sn atoms and propel Sn atoms to impinge the surface of GAF [45], resulting in the wetting of molten

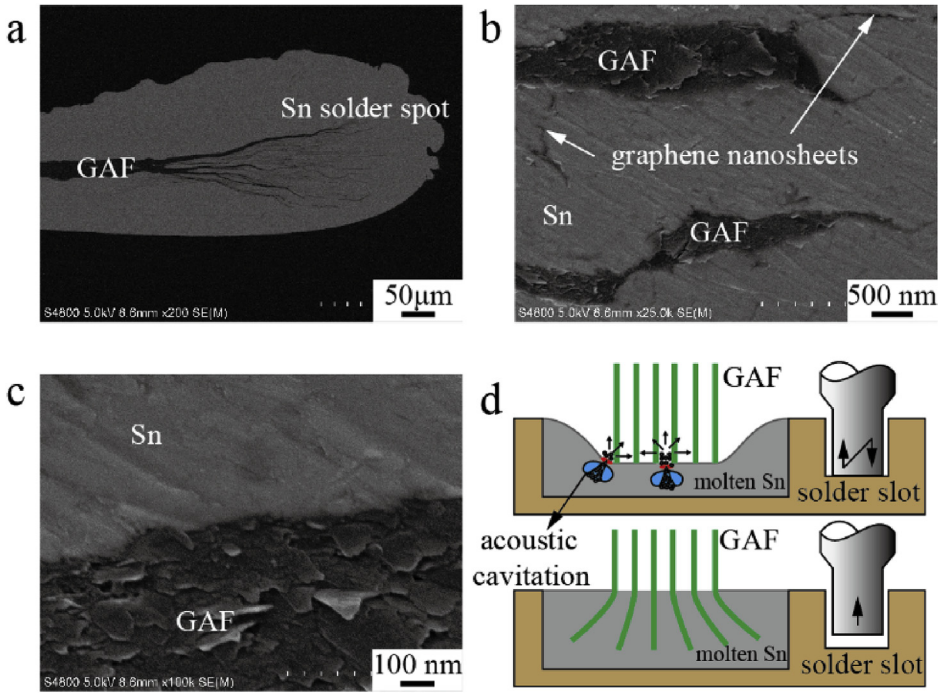

Fig. 3. (a) Cross-section image of Sn solder spot prepared on GAF surface by ultrasonic surface metallizing for 10 s at 300 °C. (b,c) Magnified SEM images of Sn/GAF interfaces. (d) Formation procedure of ramified GAF with ultrasonic assistance. (A colour version of this figure can be viewed online.)

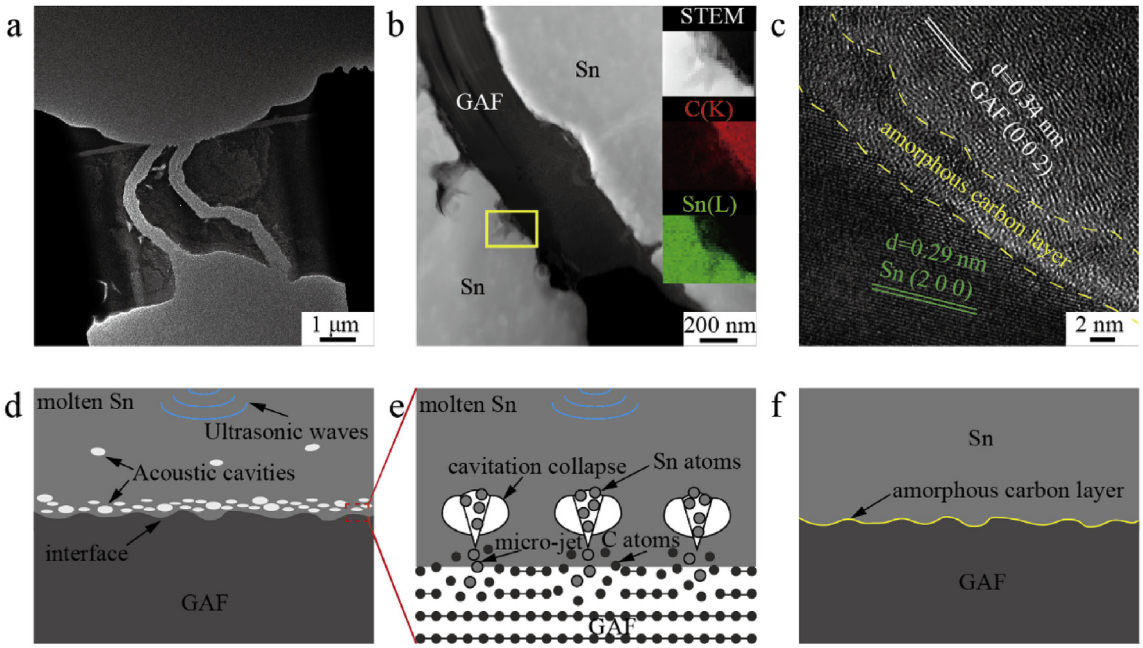

Fig. 4. Bonding mechanism between GAF and Sn solder spot. (a) Image of TEM samples. (b) HADDF-STEM image of GAF/Sn interface and EDX elemental mappings of the yellow marked region. (c) HRTEM image of GAF/Sn interface, a continuous a-C layer outlined by yellow dotted lines is formed at the interface. (d–f) Schematic diagram of a-C layer formation procedure. (A colour version of this figure can be viewed online.)

Sn on GAF surface. Due to the weak interlayer bonding of GAF [16,46], the stacked structure of GAF can be ramified under the impact of shock waves and liquid micro-jets. The exfoliation of graphene nanosheets from GAF caused by ultrasonic waves [47,48] can exacerbate unsmoothness of Sn/GAF interface. Hence, the ramified structure of GAF in macroscale and rough GAF/Sn interface in microscale can dramatically increase the contact area between GAF and Sn solder spot, which may improve the connection stability and decrease the contact resistance.

To find out the bonding mechanism of GAF/Sn interface under the action of ultrasonic waves, a TEM sample was fabricated by means of FIB thinning. The TEM sample with a thickness of less than 100 nm remains integrity (Fig. 4a), indicating that reliable connection between GAF and Sn solder is formed. Fig. 4b displays the HADDF-STEM image of GAF/Sn interface, a distinct boundary of GF/Sn can be seen due to stable structure of graphene and its hindrance to the diffusion of metal atoms [49–51]. The TEM-EDX elements mapping images inserted in Fig. 4b demonstrate that some C atoms diffuse into Sn solder. Fig. 4c shows the HRTEM image of GAF/Sn interface. Lattice stripes with a spacing of 0.34 nm are (0 0 2) lattice planes of GAF, while lattice stripes with a spacing of 0.29 nm are (2 0 0) lattice planes of Sn crystal. Significantly, there exists a continuous amorphous layer with a thickness ranging from 2 nm to 5 nm at GAF/Sn interface, which is beyond expectation. Since the soldering temperature is above 230 °C (melting temperature of Sn solder), it is impossible for molten Sn to form amorphous phase in this study. Therefore, the amorphous layer at GAF/Sn interface is an a-C layer.

The formation of a-C layer is probably associated with ultrasonic waves, as shown in Fig. 4d–f. During ultrasonic vibration, amounts of cavitation bubbles can form near the interface of GAF/molten Sn [52]. Shock waves and micro-jets induced by acoustic cavitations can drive molten Sn shooting to the surface of GAF at a speed of 400 km/h [53,54]. Such a high velocity of Sn atoms may damage the surface structure of GAF, and then produce free C atoms and exfoliate graphene nanosheets, which would diffuse into the molten Sn under the agitation of ultrasonic waves. Multiple free C atoms and graphene nanosheets can be produced on GAF surface under the violent hitting of Sn atoms induced by continuous acoustic cavitation, resulting in the formation of the a-C layer at GAF/Sn interface. The forming of a-C layer caused by bombarding of Sn atoms toward GAF surface with acoustic cavitation impelled is similar to the creation of a-C layer prepared by carbon-ion bombardment of a diamond crystal [55].

Due to highly oriented stacked structure of GAF, CTE of GAF should be within the range from -8.0×10^{-6} K^{-1} of single layer graphene [38] to -1.5×10^{-6} K^{-1} of graphite paralleled to the basal plane [37], while CTE of Sn is 22×10^{-6} K^{-1}. Thus the large CTE mismatch between GAF and Sn solder is harmful to the interfacial reliability. Interestingly, the CTE of a-C layer ranges from 1.0×10^{-6} K^{-1} of diamond to 8.0×10^{-6} K^{-1} of average CTE of graphite [37]. Hence, as a transition layer, the a-C layer can not only form a smooth transition from covalent bond of GAF to metallic bond of Sn, but also mediate the CTE mismatch between GAF and Sn solder.

To study the connection stability, tensile breaking force was measured. Before tensile test, each piece of GAF was cut into a size of 5 mm × 15 mm by laser, and GAF/Sn/GAF joints were prepared by remelting Sn metallization layers. For comparison, SCA (DOUBLE-BOND CHEMICAL DB2013) was utilized to assemble GAFs into GAF/SCA/GAF lapped joints with an overlapping area of 5 mm × 1 mm.

Fig. 5a displays one of the GAF/Sn/GAF joints. The joint exhibits neat appearance without external defects. It can be seen in Fig. 5b that the tensile failure occurs in GAF located inside the GAF/Sn/GAF joint after tensile test. The cross-section image of the failed GAF/Sn/GAF joint is shown in Fig. 5c. Notably, the tensile failure occurs in GAF located inside the joint without breaking the bonding interface between ramified GAF and Sn solder. Fig. 5d shows one of the GAF/SCA/GAF joints. After tensile test, graphene sheets bonded with SCA are exfoliated from GAF as shown in Fig. 5e. The tensile failure of GAF/SCA/GAF joints can be attributed to the weak bonding force of GAF interlayers (exfoliation tendency), as schematically shown in

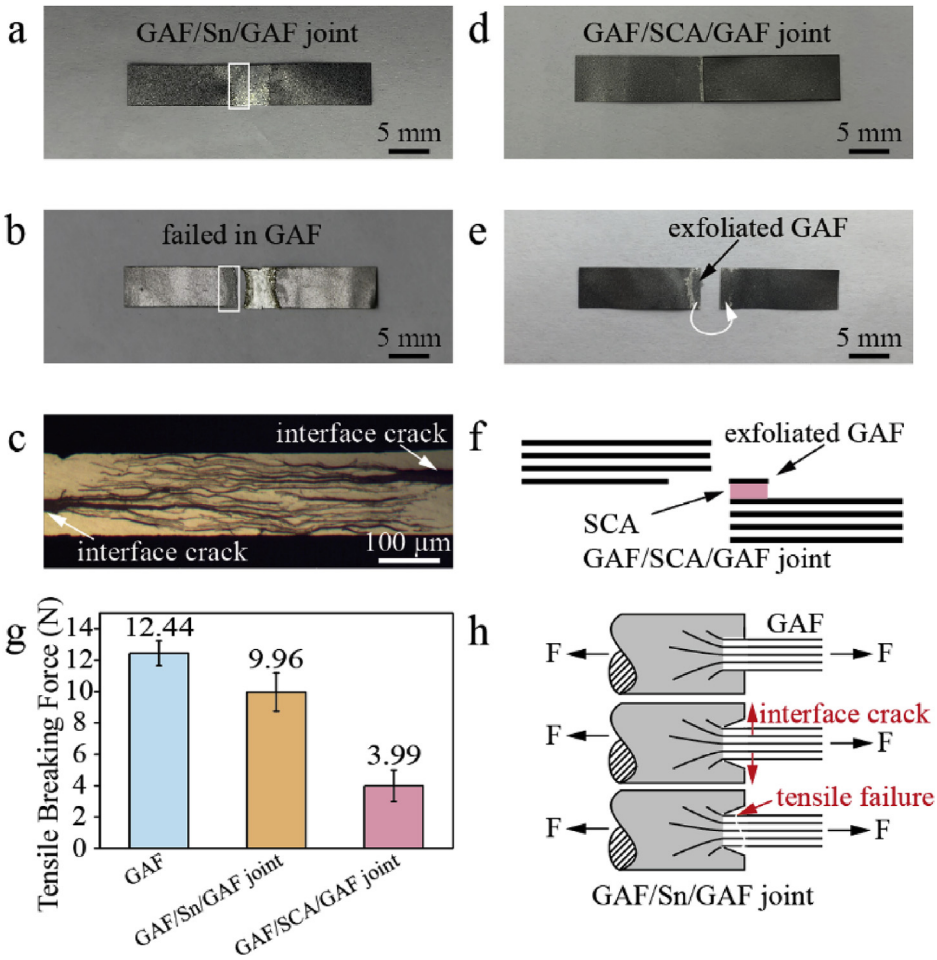

Fig. 5. Tensile strength test. (a) Photograph of a typical GAF/Sn/GAF joint prepared by remelting Sn solder spots, which were fabricated by ultrasonic surface metallizing for 10 s at 300 °C. (b) Photograph of the tensile failed GAF/Sn/GAF joint. (c) Cross-section image of tensile failed GAF/Sn/GAF joint. (d) Photograph of a typical GAF/SCA/GAF joint. (e) Photograph of tensile failed GAF/SCA/GAF joint. (f) Schematic diagram of tensile failure procedure of GAF/SCA/GAF joint. (g) Average tensile breaking forces of GAFs, GAF/Sn/GAF joints and GAF/SCA/GAF joints. (h) Schematic diagram of tensile failure procedure of GAF/Sn/GAF joint. (A colour version of this figure can be viewed online.)

Fig. 5f. Fig. 5g shows that the average tensile breaking force of GAFs, GAF/Sn/GAF joints and GAF/SCA/GAF joints are 12.44 N, 9.96 N and 3.99 N respectively. The average tensile breaking force of GAF/Sn/GAF joints is reduced by 19.9% compared with that of GAF, while the average tensile breaking force of GAF/Sn/GAF joints is approximately 150% higher than that of GAF/SCA/GAF joints.

Fig. 5h exhibits the tensile failure procedure of GAF/Sn/GAF joint. The ramified structure of GAF located inside the Sn solder and the large rough contact interface of GAF/Sn construct the interlock system between GAF and Sn solder. The interlock system may prevent GAF interlayers from exfoliating, and then enhance the tensile strength of GAF/Sn/GAF joints. Furthermore, the a-C layer at GAF/Sn interface can mediate the mismatch in lattice and CTE between GAF and Sn, which may further improve the bonding stability. Under tensile force, cracks appear first at the boundry between GAF and Sn solder, and then grow toward the direction of ramified GAF due to mismatch of elastic modulus. When encountering the branches of ramified GAF, the growth of cracks is inhibited. In addition, the thickness of GAF may decrease because of surface destruction and exfoliation caused by ultrasonic waves, so that the tensile failure tends to happen in the thinner region of GAF located inside Sn solder. The different failure mechanisms of GAF/Sn/GAF joints and GAF/SCA/GAF joints suggest that the GAF/Sn/GAF joints bonded with ultrasonic assistance can overcome the exfoliation tendency of GAF.

To test the electrical conductivity, the resistance of GAF with Sn solder spots was measured by multimeter. As shown in Fig. S3 in supporting information, the resistance of GAF with Sn solder spots is reduced by half compared with GAF without Sn solder spots, and can keep stable during repeated bending and folding. To further study the electrical conductivity of GAF joints, we designed two circuits as shown in Fig. 6a and b. Detailed fabricating process and parameter of circuits can be found in Fig. S5 in supporting information. In A-Sn and A-SCA circuits, Sn solder spots or SCA spots are prepared on all ends of the GAF to connect power leads and red LEDs. While in B—Sn and B-SCA circuits, thirty GAF/Sn/GAF or GAF/SCA/GAF joints are prepared to amplify resistance effect. Fig. 6c exhibits the current under the voltage of 2.5 V in A-Sn, A-SCA, B—Sn and B-SCA circuits. Compared with the current in A-Sn circuit under the voltage of 2.5 V, lower current in A-SCA circuit demonstrates that the Sn solder spots exhibit lower contact resistance between GAF and leads than SCA spots do. Notably, slight current difference between A-Sn and B—Sn circuits declares that the GAF/Sn/GAF joints exhibit excellent electrical conductivity, and the large difference of current between A-SCE and B-SCE suggests lower electrical conductivity of GAF/SCA/GAF joints. In addition, the wide difference of current between B—Sn and B-SCA circuits further declares the superiority of soldering technology for GAF with ultrasonic assistance. Fig. 6d shows the current under the voltage of 2.5 V in B—Sn and B-SCA circuits kept at

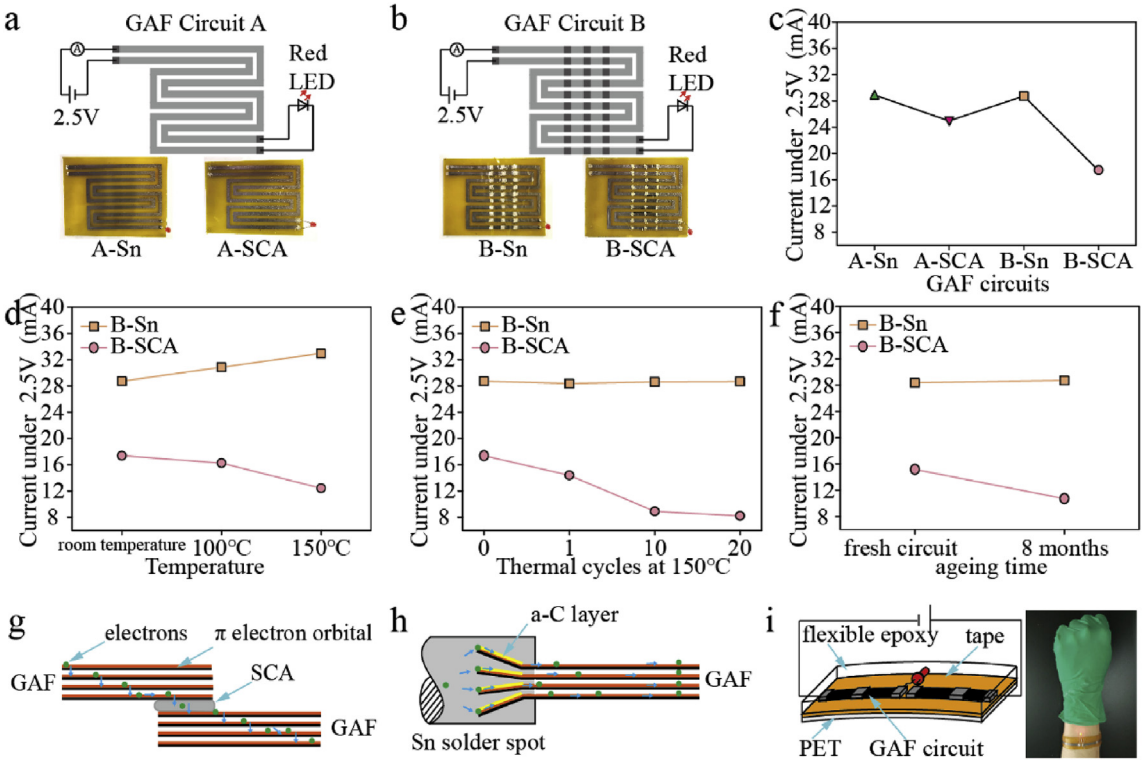

Fig. 6. Electrical conductivity test. (a) Image of GAF circuit A which consists of directed-current (DC) power, ampere meter, two pieces of continuous GAF with specific shapes and a red LED, the red LED and DC power are connected to GAF by SCA or Sn solder spots. (b) Image of GAF circuit B, which has the same components with circuit A except 30 SCA joints or Sn joints in the middle of circuit. (c) Line chart of current under the voltage of 2.5 V in A-Sn, A-SCA, B–Sn and B-SCA circuits. (d) Current under the voltage of 2.5 V in B–Sn and B-SCA circuits at room temperature, 100 °C and 150 °C, respectively. (e) Current under the voltage of 2.5 V in B–Sn and B-SCA circuits after thermal cycles from room temperature to 150 °C for different times. (f) Current variation under the voltage of 2.5 V in B–Sn and B-SCA circuits after ageing at room temperature for 8 months. (g, h) Schematic diagrams of electrons movement in GAF/SCA/GAF joint and GAF/Sn/GAF joint respectively. (i) Potential application of soldering for GAF with ultrasonic assistance in flexible GAF circuit. (A colour version of this figure can be viewed online.)

room temperature, 100 °C and 150 °C respectively. As increasing temperature, the electrical conductivity of B–Sn circuit is slightly enhanced, while that of B-SCA circuit is significantly decreased. Fig. 6e illustrates the current under the voltage of 2.5 V in B–Sn and B-SCA circuits after thermal cycling from room temperature to 150 °C for different times. With increasing thermal cycles, the electrical conductivity of B–Sn circuit can keep steady while that of B-SCA circuit decreases dramatically. Moreover, after aging at room temperature in air for 8 months, the electrical conductivity of B–Sn circuit stays unchanged while that of B-SCA circuit is reduced significantly (Fig. 6f). Thus, the GAF/Sn/GAF soldered joints prepared by remelting Sn metallization layers exhibits excellent thermal and ageing stability.

Obviously, the ramified structure of GAF inside Sn solder, and the metallurgic bonding of Sn/GAF interface by the formation of a-C layer, are most probably behind the excellent electrical conductivity of GAF/Sn/GAF joints. Compared with external connection of GAF by SCA (Fig. 6g), the penetration connection between GAF and Sn solder exhibits larger contact area, resulting in lower contact resistance. Moreover, as shown in Fig. 3a–c, 4c and 6h, Sn solder can contact with every layer of GAF, and there exsits no defects at GAF/Sn interface. Hence less electrons scattering would occur when electrons transfer between GAF interlayers, displaysing lower electrical resistance on macroscopic scale. This suggests that the GAF joints bonded by Sn with ultrasonic assistance can reduce the electrical loss between GAF interlayers. Although the resistivity of a-C layer at room temperature is as high as about 0.1 Ω cm [56], the resistance of a-C layer with a thickness of 2–5 nm is estimated to be less than 10^{-6} Ω (the derivation process is shown in supporting information), which suggests negligible influence of a-C layer on electrical conductivity. Furthermore, measured by four-probe detection method [12], the resistivity of Sn solder is 0.11×10^{-6} Ω m while the resistivity of SCA is 21.8×10^{-6} Ω m, the lower resistivity of filler materials can be conducive to improve the electrical conductivity of joint. As a result, excellent electrical conductivity is obtained for GAF/Sn/GAF joints bonded with ultrasonic assistance.

In Fig. 6i, a simple wearable GAF circuit is encapsulated by flexible epoxy, and the wearable GAF circuit involving Sn solder spots and GAF/Sn/GAF joints can adapt human wrist, showing the potential application of ultrasonic surface metallization for GAF assemblies in wearable devices.

4. Conclusion

In conclusion, we have successfully prepared flexible GAF and realized rapid soldering of GAF at low temperature in air with an ultrasonic assisted surface metallization treatment, and overcome the exfoliation tendency and electrical loss resulted from anisotropy of GAF. With ultrasonic assistance, shock waves and micro-jets induced by ultrasonic waves were supposed to improve the poor wettability of GAF surface, which drove molten Sn to penetrate into GAF interlayers to form ramified structure of GAF, and propelled Sn atoms to impinge GAF surface to form an a-C layer at Sn/GAF bonding interface, forming a smooth transition of lattice from GAF to Sn and mediating the CTE mismatch between GAF and Sn. The tensile resistance and electrical conductivity of GAF/Sn/GAF soldered joints were much higher than that of GAF joints bonded with SCA. Moreover, we found that the GAF/Sn/GAF soldered joints

exhibited excellent thermal and ageing stabilities. We believe that this bonding method can be extended to other carbon based materials (e.g., graphite, CNTs, graphene foams and carbon fibers) and materials with stratified structure or wetting obstacles, which may promote the further development of high-performance carbon-based materials devices for electronic industry.

Author contribution

Yong Xiao and Daping He conceived the project. Rongguo Song, Zhe Wang and Huaqiang Fu synthesized the graphene assembled films. Huaqiang Fu, Yong Xiao and Hongjun Ji designed and performed the ultrasonic metallizing of graphene assembled films. Huaqaing Fu and Rongguo Song performed the characterizations and carried out the electrical conductivity test. Huaqiang Fu and Yong Xiao carried out tensile test. Huaqiang Fu wrote the paper. Yong Xiao and Daping He revised the paper.

Declaration of competing interest

The authors declare that they have no known competing financial interests or personal relationships that could have appeared to influence the work reported in this paper.

Acknowledgements

This work was supported by National Natural Science Foundation of China of China (No. 51605357), and research fund of Materials Research and Analysis Center, WHUT (No. 2018KFJJ05). The authors are grateful to Dr. Zhi Zhang from Huazhong University of Science and Technology and Dr. Xiaoqing Liu from Wuhan University of Technology for their help in FIB sample preparation and TEM characterization.

Appendix A. Supplementary data

Supplementary data to this article can be found online at https://doi.org/10.1016/j.carbon.2019.11.089.

References

[1] L. Peng, Z. Xu, Z. Liu, Y. Guo, P. Li, C. Gao, Ultrahigh thermal conductive yet superflexible graphene films, Adv. Mater. 29 (2017) 1700589.
[2] S. Wan, Y. Chen, Y. Wang, G. Li, G. Wang, L. Liu, et al., Ultrastrong graphene films via long-chain π-bridging, Matter 1–13 (2019).
[3] Y. Liu, M. Yang, K. Pang, F. Wang, Z. Xu, W. Gao, et al., Environmentally stable macroscopic graphene film with specific electrical conductivity exceeding metals, Carbon 156 (2020) 205–211.
[4] R. You, Y. Liu, Y. Hao, D. Han, Y. Zhang, Z. You, Laser fabrication of graphene-based flexible electronics, Adv. Mater. (2019) 1901981.
[5] W. Liu, N. Liu, Y. Yue, J. Rao, F. Cheng, J. Su, et al., Piezoresistive pressure sensor based on synergistical innerconnect polyvinyl alcohol nanowires/wrinkled graphene film, Small 14 (2018) 1704149.
[6] K. Xia, C. Wang, M. Jian, Q. Wang, Y. Zhang, CVD growth of fingerprint-like patterned 3D graphene film for an ultrasensitive pressure sensor, Nano Res 11 (2018) 1124–1134.
[7] M. Zhang, J.T.W. Yeow, A flexible, scalable, and self-powered mid-infrared detector based on transparent PEDOT: PSS/graphene composite, Carbon 156 (2020) 339–345.
[8] Y. Qiao, Y. Wang, J. Jian, M. Li, G. Jiang, Multifunctional and high-performance electronic skin based on silver nanowires bridging graphene, Carbon 156 (2020) 253–260.
[9] Z. Xiong, C. Liao, W. Han, X. Wang, Mechanically tough large-area hierarchical porous graphene films for high-performance flexible supercapacitor applications, Adv. Mater. 27 (2015) 4469–4475.
[10] B. Xie, C. Yang, Z. Zhang, P. Zou, Z. Lin, G. Shi, et al., Shape-tailorable graphene-based ultra-high-rate supercapacitor for wearable electronics, ACS Nano 9 (2015) 5636–5645.
[11] A. Scidà, S. Haque, E. Treossi, A. Robinson, S. Smerzi, S. Ravesi, et al., Application of graphene-based flexible antennas in consumer electronic devices, Mater. Today 21 (2018) 223–230.
[12] R. Song, Q. Wang, B. Mao, Z. Wang, D. Tang, B. Zhang, et al., Flexible graphite films with high conductivity for radio-frequency antennas, Carbon 130 (2018) 164–169.
[13] D. Tang, Q. Wang, Z. Wang, Q. Liu, B. Zhang, D. He, et al., Highly sensitive wearable sensor based on a flexible multi-layer graphene film antenna, Sci. Bull. 63 (2018) 574–579.
[14] F.J. Tölle, M. Fabritius, R. Mülhaupt, Emulsifier-free graphene dispersions with high graphene content for printed electronics and freestanding graphene films, Adv. Funct. Mater. 22 (2012) 1136–1144.
[15] Q. Cui, F. Gao, S. Mukherjee, Z. Gu, Joining and Interconnect formation of nanowires and carbon nanotubes for nanoelectronics and nanosystems, Small 5 (2009) 1246–1257.
[16] G. Wang, Z. Dai, Y. Wang, P. Tan, L. Liu, Z. Xu, et al., Measuring interlayer shear stress in bilayer graphene, Phys. Rev. Lett. 119 (2017), 036101.
[17] C. Ramirez, L. Garzón, P. Miranzo, M.I. Osendi, C. Ocal, Electrical conductivity maps in graphene nanoplatelet/silicon nitride composites using conducting scanning force microscopy, Carbon 49 (2011) 3873–3880.
[18] X. Huang, T. Leng, X. Zhang, J.C. Chen, K.H. Chang, A.K. Geim, et al., Binder-free highly conductive graphene laminate for low cost printed radio frequency applications, Appl. Phys. Lett. 106 (2015) 203105.
[19] E.J. Kim, V.H. Luan, H.N. Tien, B.-S. Kong, T.V. Cuong, S.H. Hur, et al., Novel conductive epoxy composites composed of 2-D chemically reduced graphene and 1-D silver nanowire hybrid fillers, J. Mater. Chem. 22 (2012) 8649–8653.
[20] J. Luo, Z. Cheng, C. Li, L. Wang, C. Yu, Y. Zhao, Electrically conductive adhesives based on thermoplastic polyurethane filled with silver flakes and carbon nanotubes, Compos. Sci. Technol. 129 (2016) 191–197.
[21] M.T. Barako, Y. Gao, A.M. Marconnet, M. Asheghi, K.E. Goodson, Solder-bonded carbon nanotube thermal interface materials, in: 13th InterSociety Conference on Thermal and Thermomechanical Phenomena in Electronic Systems, IEEE, San Diego, 2012, pp. 1225–1233.
[22] M. Burda, A. Lekawa-Raus, A. Gruszczyk, K.K.K. Koziol, Soldering of carbon materials using transition metal rich alloys, ACS Nano 9 (2015) 8099–8107.
[23] Y. Liu, C. Liang, A. Wei, Y. Jiang, Q. Tian, Y. Wu, et al., Solder-free electrical Joule welding of macroscopic graphene assemblies, Mater. Today Nano 3 (2018) 1–8.
[24] G. Çam, M. Koçak, Progress in joining of advanced materials, Int. Mater. Rev. 43 (1998) 1–44.
[25] J. Wang, K. Li, W. Li, H. Li, Z. Li, L. Guo, The preparation and mechanical properties of carbon/carbon composite joints using Ti-Si-SiC-C filler as interlayer, Mater. Sci. Eng. A 574 (2013) 37–45.
[26] W. Guo, Y. Zhu, L. Wang, P. Qu, H. Kang, P.K. Chu, Microstructure evolution and mechanical properties of vacuum-brazed C/C composite with AgCuTi foil, Mater. Sci. Eng. A 564 (2013) 192–198.
[27] T Te Chou, W.H. Tuan, H. Nishikawa, B.J. Weng, Brazing graphite to aluminum nitride for thermal dissipation purpose, Adv. Eng. Mater. 19 (2017) 1–6.
[28] A.K. GEIM, K.S. NOVOSELOV, The rise of graphene, Nat. Mater. 6 (2007) 183–191.
[29] S. Chen, Q. Wu, C. Mishra, J. Kang, H. Zhang, K. Cho, et al., Thermal conductivity of isotopically modified graphene, Nat. Mater. 11 (2012) 203–207.
[30] H. Wang, J. Cao, J. Feng, Brazing mechanism and infiltration strengthening of CC composites to TiAl alloys joint, Scr. Mater. 63 (2010) 859–862.
[31] J. Zhang, T. Wang, C. Liu, Y. He, Effect of brazing temperature on microstructure and mechanical properties of graphite/copper joints, Mater. Sci. Eng. A 594 (2014) 26–31.
[32] H. Bai, C. Xue, J.L. Lyu, J. Li, G.X. Chen, J.H. Yu, et al., Thermal conductivity and mechanical properties of flake graphite/copper composite with a boron carbide-boron nano-layer on graphite surface, Compos. Part A Appl. Sci. Manuf. 106 (2018) 42–51.
[33] R. Zhang, X. He, Z. Chen, X. Qu, Influence of Ti content on the microstructure and properties of graphite flake/Cu-Ti composites fabricated by vacuum hot pressing, Vacuum 141 (2017) 265–271.
[34] Y. Huang, Y. Su, S. Li, Q. Ouyang, G. Zhang, L. Zhang, et al., Fabrication of graphite film/aluminum composites by vacuum hot pressing: process optimization and thermal conductivity, Compos. B Eng. 107 (2016) 43–50.
[35] X.G. Song, J.H. Chai, S.P. Hu, J. Cao, J.C. Feng, D.Y. Tang, A novel metallization process for soldering graphite to copper at low temperature, J. Alloy. Comp. 696 (2017) 1199–1204.
[36] W. Fu, S.P. Hu, X.G. Song, J.X. Li, J. Cao, J.C. Feng, et al., Wettability and bonding of graphite by Sn0.3Ag0.7Cu-Ti alloys, Carbon 121 (2017) 536–543.
[37] G.A.J. Amaratunga, I. Andrienko, J.V. Anguita, M. Aono, W. Arnold, R.C. Barklie, et al., Properties of Amorphous Carbon, 29th ed., The Institution of Electrical Engineers, London, 2003.
[38] D. Yoon, Y.W. Son, H. Cheong, Negative thermal expansion coefficient of graphene measured by Raman spectroscopy, Nano Lett. 11 (2011) 3227–3231.
[39] Z. Wang, G. Wang, M. Li, J. Lin, Q. Ma, A. Zhang, et al., Three-dimensional graphene-reinforced Cu foam interlayer for brazing C/C composites and Nb, Carbon 118 (2017) 723–730.
[40] S. Reich, C. Thomsen, Raman spectroscopy of graphite, Philos. Trans. R. Soc. Lond. Ser. A Math. Phys. Eng. Sci. 362 (2004) 2271–2288.
[41] X. Dong, H. Xu, H. Chen, L. Wang, J. Wang, W. Fang, et al., Commercial expanded graphite as high-performance cathode for low-cost aluminum-ion battery, Carbon 148 (2019) 134–140.
[42] S.A. Sánchez, J. Narciso, E. Louis, F. Rodríguez-Reinoso, E. Saiz, A. Tomsia, Wetting and capillarity in the Sn/graphite system, Mater. Sci. Eng. A 495 (2008) 187–191.

[43] L.X. Zhang, Q. Chang, Z. Sun, J.J. Zhang, J.L. Qi, J.C. Feng, Wetting of AgCuTi alloy on quartz fiber reinforced composite modified by vertically aligned carbon nanotubes, Carbon 154 (2019) 375–383.
[44] K.S. Suslick, The chemical effects of ultrasound, Sci. Am. 80–6 (1989).
[45] D. Luo, Y. Xiao, L. Wang, L. Liu, X. Zeng, M. Li, Interfacial reaction behavior and bonding mechanism between liquid Sn and ZrO2ceramic exposed in ultrasonic waves, Ceram. Int. 43 (2017) 7531–7536.
[46] J.C. Charlier, X. Gonze, J.P. Michenaud, Graphite interplanar bonding: electronic delocalization and van der waals interaction, Epl 28 (1994) 403–408.
[47] M. Noroozi, A. Zakaria, S. Radiman, Z.A. Wahab, Environmental synthesis of few layers graphene sheets using ultrasonic exfoliation with enhanced electrical and thermal properties, PLoS One 11 (2016) 1–17.
[48] V. Sharma, A. Garg, S.C. Sood, Graphene synthesis via exfoliation of graphite by ultrasonication, Int. J. Eng. Trends Technol. 26 (2015) 38–42.
[49] Y.H. Ko, J.D. Lee, T. Yoon, C.W. Lee, T.S. Kim, Controlling interfacial reactions and intermetallic compound growth at the interface of a lead-free solder joint with layer-by-layer transferred graphene, ACS Appl. Mater. Interfaces 8 (2016) 5679–5686.
[50] Y. Gan, L. Sun, F. Banhart, One- and two-dimensional diffusion of metal atoms in graphene, Small 4 (2008) 587–591.
[51] X.D. Liu, Y.D. Han, H.Y. Jing, J. Wei, L.Y. Xu, Effect of graphene nanosheets reinforcement on the performance of Sn-Ag-Cu lead-free solder, Mater. Sci. Eng. A 562 (2013) 25–32.
[52] D.G. Shchukin, E. Skorb, V. Belova, H. Möhwald, Ultrasonic cavitation at solid surfaces, Adv. Mater. 23 (2011) 1922–1934.
[53] W. Weng, V.G. Pol, K. Amine, Ultrasound assisted design of sulfur/carbon cathodes with partially fluorinated ether electrolytes for highly efficient Li/S batteries, Adv. Mater. 25 (2013) 1608–1615.
[54] R.L. Zhang, X.F. Zhang, S.Z. Tang, A.D. Huang, Ultrasound-assisted HCl-NaCl leaching of lead-rich and antimony-rich oxidizing slag, Ultrason. Sonochem. 27 (2015) 187–191.
[55] J.J. Hauser, J.R. Patel, Hopping conductivity in C-implanted amorphous diamond, or how to ruin a perfectly good diamond, Solid State Commun. 18 (1976) 789–790.
[56] J.J. Hauser, Hopping conductivity in amorphous carbon films, Solid State Commun. 17 (1975) 1577–1580.